ACS NANO

www.acsnano.org

ARTICLE

Charge-Transfer-Induced Interfacial Ferromagnetism in Ferromagnet-Free Oxide Heterostructures

Jie Zheng, Wenxiao Shi, Zhe Li, Jing Zhang,* Chao-Yao Yang, Zhaozhao Zhu, Mengqin Wang, Jine Zhang, Furong Han, Hui Zhang, Yunzhong Chen, Fengxia Hu, Baogen Shen, Yuansha Chen,* and Jirong Sun*

Cite This: *ACS Nano* 2024, 18, 9232−9241

Read Online

ACCESS | Metrics & More | Article Recommendations | Supporting Information

ABSTRACT: **Due to the strong interlayer coupling between multiple degrees of freedom, oxide heterostructures have demonstrated exotic properties that are not shown by their bulk counterparts. One of the most interesting properties is ferromagnetism at the interface formed between "nonferromagnetic" compounds. Here we report on the interfacial ferromagnetic phase induced in the superlattices consisting of the two paramagnetic oxides $CaRuO_3$ (CRO) and $LaNiO_3$ (LNO). By varying the sublayer thickness in the superlattice period, we demonstrate that the ferromagnetic order has been established in both $CaRuO_3$ and $LaNiO_3$ sublayers, exhibiting an identical Curie temperature of ∼75 K. The X-ray absorption spectra suggest a strong charge transfer from Ru to Ni at the interface, triggering superexchange interactions between Ru/Ni ions and giving rise to the emergent ferromagnetic phase. Moreover, the X-ray linear dichroism spectra reveal the preferential occupancy of the $d_{3z^2-r^2}$ orbital for the Ru ions and the $d_{x^2-y^2}$ orbital for the Ni ions in the heterostructure. This leads to different magnetic anisotropy of the superlattices when they are dominated by CRO or LNO sublayers. This work clearly demonstrates a charge-transfer-induced interfacial ferromagnetic phase in the whole ferromagnet-free oxide heterostructures, offering a feasible way to tailor oxide materials for desired functionalities.**

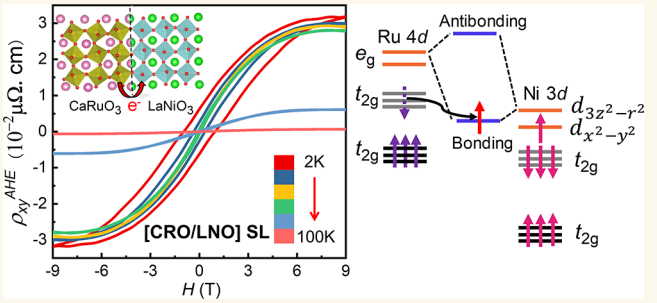

KEYWORDS: *$CaRuO_3$, $LaNiO_3$, charge transfer, orbital reconstruction, interfacial ferromagnetism*

INTRODUCTION

ABO_3-type perovskite transition-metal oxides (TMOs) have exhibited a wide variety of fascinating properties due to their strongly correlated d-band electrons, including high-T_c superconductivity, colossal magnetoresistance, ferroelectricity, and multiferroicity.[1−4] Benefiting from the advances in deposition techniques, it becomes possible to get precisely controlled heterostructures composed of different oxides.[5] The heterointerfaces usually exhibit exotic properties different from their bulk constituents due to the existence of coupled degrees of freedom, providing a promising platform for the exploration of emergent quantum states.[6] Thus, intensive research effort has been devoted to the design of artificial oxide heterostructures, particularly regarding the effect of interface coupling. Charge reconstruction at oxide interfaces is a common feature that has led to abundant intriguing phenomena such as interfacial superconductivity, interfacial magnetism, and unexpected magnetic anisotropy.[7−10] When two oxides with different electronegativities are in close contact, the hybridization of adjacent atomic orbitals produces low-lying molecular orbitals, causing interfacial charge transfer to balance the band offset of the two oxides.[11] Along with the charge reconstruction, interlayer exchange interaction may also occur, aligning the spin of two types of TM ions at the interface according to the Goodenough−Kanamori−Anderson rules.[12−14] Such an interlayer interaction will transfer the magnetic order from the ferromagnetic/antiferromagnetic (FM/AFM) layers to adjacent nonmagnetic layers. For example, by the proximity to FM $La_{0.7}Sr_{0.3}MnO_3$, $LaMnO_3$, or $LaCoO_3$ layers, the FM order was

Received: February 7, 2024
Revised: March 1, 2024
Accepted: March 7, 2024
Published: March 11, 2024

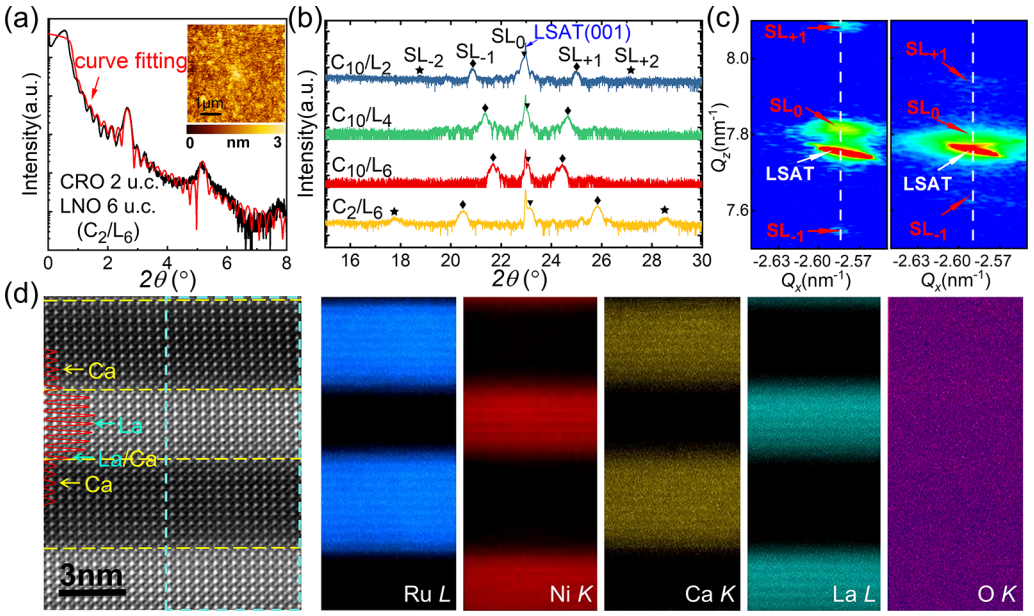

Figure 1. Structural characterization of CRO/LNO SLs. (a) XRR intensity oscillations (black line) of the C_2/L_6 SL. The red line is the simulation curve. The inset plot shows the atomic force microscopy image of this sample. (b) High-resolution θ–2θ patterns of C_n/L_m SLs on LSAT. SL_0 indicates (001) main peak, and SL_{-1}, SL_{+1}, SL_{-2}, and SL_{+2} indicate satellite peaks. (c) RSM around the pseudocubic (103) reflection for the C_2/L_6 and C_{10}/L_6 SLs on LSAT substrate. (d) HAADF image of the cross-section of the C_{10}/L_8 SL, recorded along the [100] zone axis. The interface between CRO and LNO is denoted by the dashed horizontal lines marked in yellow. The right panel shows the energy-dispersive X-ray spectroscopy (EDS) mappings of Ru, Ni, Ca, La, and O elements in the SL, respectively, acquired from the blue dashed box.

successfully induced in paramagnetic (PM) $SrIrO_3$ or $LaNiO_3$ (LNO) layers,[15−17] via the so-called magnetic proximity effect. Emergent interfacial FM phases were also observed in the PM/AFM combinations, such as $LaNiO_3/CaMnO_3$, $CaRuO_3$(CRO)/$CaMnO_3$, and $SrIrO_3/SrMnO_3$, where the itinerant electron-mediated double-exchange interaction was considered as the mechanism.[7,18−20] These results are of great significance since the interfacial ferromagnetism has an obvious advantage over the bulk counterpart, considering the fact that the low-dimensional characteristics are highly desired for technological applications in sensors or memory devices. However, the existence of an FM or AFM layer in the PM/FM or PM/AFM heterostructures would induce a strong pinning effect to the interfacial magnetic state, resulting in considerable restriction on the manipulation of magnetic moment. If the interfacial FM phase can be generated in the heterostructures consisting of two nonmagnetic constituents, the magnetic moment would become more tunable. For example, effective tuning of a magnetic easy axis for an interfacial FM phase was achieved in the CRO/$SrTiO_3$ superlattice (SL) just by varying the thickness of sublayers, showing potential applications in low-power-consumption or exchange spring devices.[21]

In this paper, we pay attention to a special superlattice (SL) formed by two typical PM oxides: the 4d ruthenate CRO and 3d nickelate LNO. CRO is an orthorhombically structured PM metal, showing non-Fermi-liquid behavior at low temperatures.[22] In comparison with its sister system, the itinerant ferromagnet $SrRuO_3$ (SRO), CRO has a larger orthorhombic distortion, which causes the degeneracy of t_{2g} band and a relatively low density of states $N(E_F)$ near the Fermi surface.[23,24] As a result, CRO remains PM down to 2 K in either bulk or thin film forms.[25,26] Different from CRO, LNO is rhombohedrally structured. It is a metallic Pauli paramagnet that lacks any magnetic order over the temperature range of 2−300 K.[27] This is quite different from other rare-earth nickelates (such as $NdNiO_3$, $PrNiO_3$) that usually possess an insulating AFM ground state at low temperature.[28,29] Therefore, the development of magnetic order in LNO has attracted great attention since the discovery of the unexpected magnetic pinning effect of LNO layers to the neighboring $LaMnO_3$ layers.[17,30,31]

Here, we report on the interfacial FM phase in the PM-CRO/PM-LNO SLs epitaxially grown on (001)-orientated $(LaAlO_3)_{0.3}$-$(Sr_2AlTaO_6)_{0.7}$ (LSAT) substrates. An anomalous Hall effect (AHE) and butterfly-shaped magnetoresistance loops are observed in all the SLs investigated, regardless of whether the transport behavior of SL is dominated by the CRO or the LNO sublayers in various thickness combinations of the SL period. It suggests that both the CRO and LNO sublayers in the heterostructures have become FM, exhibiting an identical Curie temperature (T_c) of ∼75 K. The X-ray absorption and linear dichroism spectra confirm the strong charge transfer from Ru to Ni at the CRO/LNO interface, resulting in a preferential occupancy of the $d_{3z^2-r^2}$ orbital for Ru ions and the $d_{x^2-y^2}$ orbital for Ni ions. This well explains the perpendicular magnetic anisotropy for the CRO-dominant SL and the in-plane magnetic anisotropy for the LNO-dominant SL. These findings offer a feasible way to induce and tune the FM phase at the PM/PM oxide heterointerface, presenting great potential in spintronics and magnetoelectronics applications.

RESULTS AND DISCUSSION

Structural Analysis of CRO_n/LNO_m Superlattices. CRO_n/LNO_m (C_n/L_m) SLs by alternately stacking CRO and LNO layers with 10 repetitions were epitaxially grown on (001)-oriented LSAT single-crystal substrates by pulsed laser deposition. Here n = 2, 10 and m = 2, 4, 6, 8 represent the

https://doi.org/10.1021/acsnano.4c01910
ACS Nano 2024, 18, 9232−9241

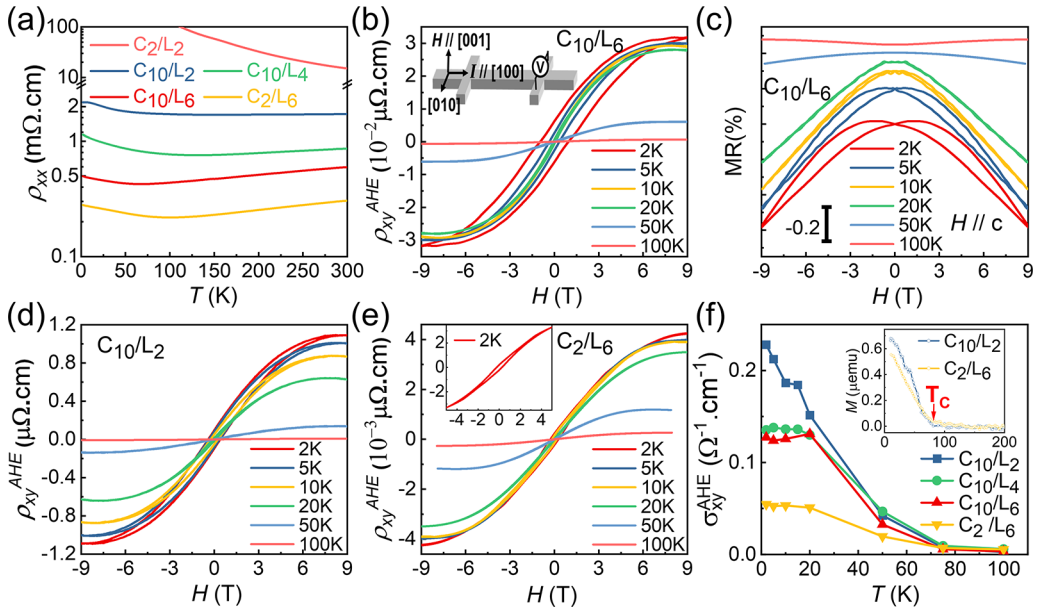

Figure 2. Magneto-transport characterization. (a) Longitudinal resistivity (ρ_{xx}) versus temperature (T) for C_n/L_m SLs. (b) Anomalous Hall resistivity (ρ_{xy}^{AHE}) and (c) magnetoresistance (MR) versus magnetic field (H) for the C_{10}/L_6 SL, measured at temperatures ranging from 2 to 100 K. The inset is a schematic view of the experimental setup for Hall measurements. The MR curves are offset along the vertical direction to prevent overlapping. H-dependent ρ_{xy}^{AHE} curves obtained from 2 to 100 K for (d) C_{10}/L_2 SL and (e) C_2/L_6 SL. The inset plot is the zoom-in view of the loops at low field at 2 K. (f) Anomalous Hall conductivity σ_{xy}^{AHE} versus T for all SLs. The inset plot is the magnetization (M) versus T for C_{10}/L_2 and C_2/L_6 SLs measured with an out-of-plane field of 0.2 T in field-cooling mode, showing the identical T_c of ~75 K.

numbers of unit cells (uc) for the CRO and LNO sublayers, respectively. The deposition rate has been carefully calibrated by the technique of small-angle X-ray reflectivity (XRR), and the thickness of each sublayer is controlled by the number of laser pulses. Figure 1a shows the XRR profile of the typical sample C_2/L_6, demonstrating clear satellite peaks, which are the distinct feature of SLs. The layer thickness deduced from curve fitting is in line with the preset value. The inset plot of Figure 1a is the surface morphology of the same sample, showing satisfactory uniformity and smoothness, as suggested by the low root-mean-square roughness (~3.7 Å). To clearly show the structure characteristics, the X-ray diffraction (XRD) spectra of the SLs are measured, and the results are presented in Figure 1b. (001) main peak (SL_0) and distinct satellite peaks ($SL_{\pm1}$, $SL_{\pm2}$) are observed, indicating the good crystallinity and well-ordered structure of the SLs. With a decrease in the CRO layer thickness or an increase in the LNO layer thickness, the SL_0 peak shifts to higher angles. This is understandable since the lattice constant of LNO is smaller than that of CRO (3.84 Å vs 3.85 Å). The separation between satellite peaks decreases with the increase of SL period thickness (nCRO + mLNO), which is a general feature of the XRD spectra of SLs. To further determine the in-plane strain state, the reciprocal space mapping (RSM) of the (103) reflection is measured. Figure 1c shows the results of the thinnest C_2/L_6 and the thickest C_{10}/L_6 SLs. The diffraction spots of the SLs (marked by red arrows) are located just above that of the LSAT substrate; i.e., the SLs are coherently strained to the substrate without lattice relaxations. This conclusion is also applicable to other samples. All these features indicate the high quality of SLs, with well-ordered target structures.

To get information about atomic scale structure, the lattice image of a C_{10}/L_8 SL is collected by a high-resolution scanning transmission electron microscope (STEM). Figure 1d is the atomically resolved high-angle annular dark-field (HAADF) image of the cross-section of the C_{10}/L_8 SL, recorded along the [100] zone axis. Due to the strong brightness contrast between Ca and La ions, the alternate stacking of CRO and LNO layers is clearly seen, confirming the epitaxial growth of the periodic structure. Regular arrays of A-site and B-site cations are observed in the HAADF image without visible dislocations or defects. The line profile analysis along the vertical direction is further shown in the inset panel. For each CRO (or LNO) layer, the brightness of the first bottom Ca−O layer (or La−O layer) is relatively higher (or lower) than that of the other layers. It suggests that partial Ca^{2+} (or La^{3+}) ions in the first layer are replaced by La^{3+} (or Ca^{2+}) ions, i.e. an A-site intermixing appears within one unit cell. The right panel of Figure 1d is the energy-dispersive X-ray spectroscopy (EDS) mapping images acquired from the blue dashed-boxed region, representing the signals of Ru−L, Ni−K, Ca-L, La−K, and O−K, respectively. The EDS results indicate that the Ca, Ru, La, and Ni ions are located at the correct position of the layered structure. The O−K mapping reveals a homogeneous oxygen content in the SL.

Emergent Ferromagnetism in CRO/LNO SLs. Though CRO and LNO bare films are well metallic, they become insulating when the film thickness is thin enough.[32−35] This gives us a chance to distinguish the contribution of the CRO or LNO sublayers to electronic transport, adopting different n/m combinations of the C_n/L_m SL. Figure 2a compares the temperature (T) dependence of the longitudinal resistivity (ρ_{xx}) for all SLs. Aside from C_2/L_2, other SLs are essentially metallic with a slight resistivity upturn at low temperatures. This resistance upturn is similar to the metal-to-insulator transitions observed in ultrathin $LaNiO_3$ and $SrRuO_3$ films as well as associated SL samples, where the interfacial scattering was enhanced; thus, the transport behaviors with the features of weak localization appeared at low temperatures.[36,37] The resistivity increases quickly with the decrease of the thickness

https://doi.org/10.1021/acsnano.4c01910
ACS Nano 2024, 18, 9232−9241

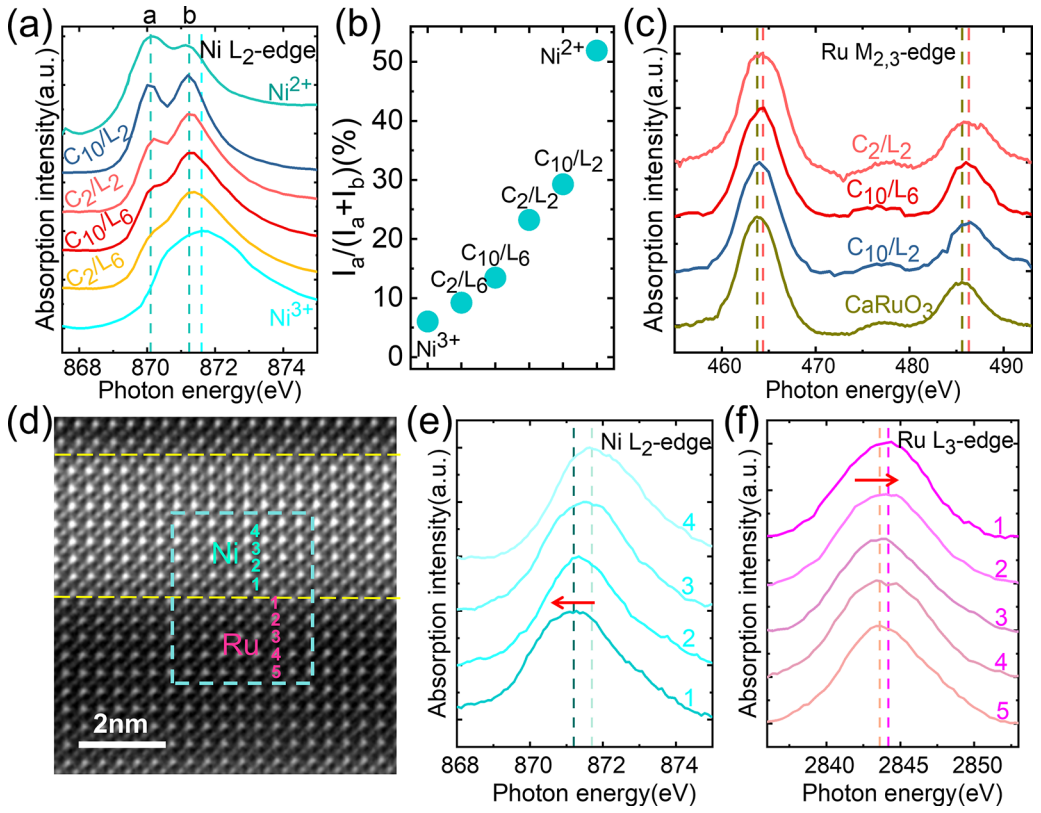

Figure 3. XAS and EELS characterizations. (a) Normalized XAS of the Ni L_2-edge for the C_n/L_m SLs and reference samples NiO and $LaNiO_3$.[40] Dashed lines are guidelines for peak positions. (b) Relative intensity of peak a in (a) plotted for the different samples. (c) Normalized XAS of the Ru $M_{2,3}$-edge for the C_n/L_m SLs and reference sample $CaRuO_3$. (d) Enlarged HAADF image of one period of the C_{10}/L_8 SL, where the EELS line profile is conducted in the dashed box along the [001] direction. (e, f) Layer-resolved EELS spectra of the Ni L_2-edge and Ru L_3-edge, respectively.

of the CRO or LNO sublayer and, finally, becomes completely semiconducting when $n = 2$ and $m = 2$. This is consistent with previous reports that the critical thickness for the LNO or CRO film to maintain its metallic behavior is at least 4 uc.[33,35] Considering that the ρ_{xx} of C_2/L_2 is 2−3 orders of magnitude greater than that of other SLs at low temperatures, it is reasonable to assume the 2-uc-thick CRO or LNO layer in the SL has a negligible contribution to metallic conductivity. The transport behavior of C_{10}/L_2 or C_2/L_6 SL is dominated by the 10-uc-thick CRO or 6-uc-thick LNO sublayers, respectively, while the transport behavior of C_{10}/L_6 SL is jointly determined by both the CRO and LNO sublayers. This inference can be further confirmed by a simple calculation based on a parallel multilayer model. Take room-temperature resistivity as an example. ρ_{300}^{CRO} of the 10-uc-thick CRO layer is ∼1.72 mΩ cm and ρ_{300}^{LNO} of the 6-uc-thick LNO layer is ∼0.30 mΩ cm, deduced from the data of C_{10}/L_2 and C_2/L_6 SLs, respectively. Based on the parallel model, the room temperature resistivity of C_{10}/L_6 SL can be obtained. It is ∼0.62 mΩ cm, close to the measured value of ∼0.60 mΩ cm.

To reveal the emergent phenomena in the C_n/L_m SL, the magnetotransport properties are further investigated using the standard Hall-bar configuration. Generally, the Hall resistivity of a ferromagnet can be described by $\rho_{xy} = R_0B + \mu_0R_sM$, where the first term represents the ordinary Hall effect that is proportional to the applied magnetic field H, and the second term represents the anomalous Hall resistivity (ρ_{xy}^{AHE}) that is proportional to the spontaneous magnetization M.[38] Figure 2b shows the ρ_{xy}^{AHE} of the C_{10}/L_6 SL as a function of H measured at different temperatures. The ordinary Hall contribution was subtracted from the total Hall signals. ρ_{xy}^{AHE}-H curve at 2 K displays clear hysteresis behavior with a coercive field (H_C) of 0.97 T. As the temperature increases from 2 to 20 K, H_C decreases rapidly while the saturation value of ρ_{xy}^{AHE} ($\Delta\rho_{xy}^{AHE}$) remains almost constant (0.03 μΩ cm). Then $\Delta\rho_{xy}^{AHE}$ significantly decreases when the temperature exceeds 20 K and, finally, disappears above 100 K. A similar temperature dependence is obtained for the magnetoresistance (MR). Figure 2c depicts the magnetic field dependence of $MR = \frac{\rho_{xx}(H) - \rho_{xx}(0)}{\rho_{xx}(0)} \times 100\%$ obtained from 2 to 100 K, where ρ_{xx} (H) and ρ_{xx} (0) are the longitudinal resistivities measured with and without an out-of-plane field H, respectively. Butterfly-shaped MR−H loops with two broad peaks at $\pm H_C$ are clearly observed at low temperatures. Similar to $\Delta\rho_{xy}^{AHE}$, the MR at 9 T keeps a negative value of ∼−0.65% in the temperature range from 2 to 20 K and then substantially decreases when the temperature exceeds 20 K and takes a small value of ∼−0.06% at 50 K. Above 100 K, MR becomes positive. The obvious AHE and MR hysteresis loops strongly suggest the establishment of a FM order in the C_{10}/L_6 SL. This is interesting, noting the fact that the individual CRO or LNO film is PM (as shown in Figure S1, the CRO and LNO bare films show no AHE and MR loops at all). The emergence of the FM phase in the SL thus should arise from the interlayer coupling effect between CRO and LNO.

To get an idea about which sublayer of the heterostructure becomes FM, Hall measurements were further performed for

https://doi.org/10.1021/acsnano.4c01910
ACS Nano 2024, 18, 9232−9241

other SL samples. As mentioned above, the transport properties of the C_{10}/L_2 or C_2/L_6 SL should be dominated by the CRO or LNO sublayers. Surprisingly, sizable ρ_{xy}^{AHE} signals are also obtained for these two SLs (Figure 2d,e). The C_{10}/L_2 SL shows obvious hysteresis loops similar to the C_{10}/L_6 SL, while the C_2/L_6 SL has much smaller H_C and $\Delta\rho_{xy}^{AHE}$. The MR–H curves of these two SLs are given in Figure S2a,b. Similar to C_{10}/L_6, C_{10}/L_2 and C_2/L_6 SLs also exhibit a negative MR and butterfly-shaped MR–H loops at low temperatures. We therefore conclude that the FM state is induced in both CRO and LNO sublayers near the CRO/LNO interface.

As reported, the intrinsic AHE is determined by the integral of Berry curvature over the occupied states in the entire Brillouin zone.[38,39] In this case, the ρ_{xy}^{AHE} follows the formula of $\rho_{xy}^{AHE} = S_H\rho_{xx}^2(H,T)M(H,T)$, where the coefficient S_H is independent of H and T. In Figure S3 in the Supporting Information, we plot $\Delta\rho_{xy}^{AHE}(T)$ as a function of $\rho_{xx}^2(T)$ for all SLs. Within the temperature range of 2–20 K, $\Delta\rho_{xy}^{AHE}(T)$ exhibits a good linear dependence on $\rho_{xx}^2(T)$ for the C_{10}/L_6, C_{10}/L_4, and C_2/L_6 SLs, indicating that the AHE of these samples originates from Berry curvature. The deviation from linearity of the $\Delta\rho_{xy}^{AHE}(T)$–$\rho_{xx}^2(T)$ curve for the C_{10}/L_2 SL can be ascribed to the increase of magnetization when the temperature varies from 20 to 2 K (Figure S3). In Figure 2f, we plot the anomalous Hall conductivity σ_{xy}^{AHE} as a function of temperature for all SLs, where $\sigma_{xy}^{AHE}(T)$, defined as $\sigma_{xy}^{AHE}(T) = \frac{\Delta\rho_{xy}^{AHE}(T)}{\rho_{xx}^2(T)} = S_H M$, is proportional to magnetization M. As shown in Figure 2f, the $\sigma_{xy}^{AHE}(T)$ values of different SLs show consistent magnetic features, displaying similar critical temperatures and saturation temperatures. This implies that the FM CRO and LNO sublayers are strongly coupled together at the interface. The reduction of σ_{xy}^{AHE} with the decrease of n or the increase of m for the C_n/L_m SL possibly implies that the LNO sublayer has a much lower anomalous Hall conductivity than the CRO sublayer. To further determine T_c, the temperature dependence of magnetization (M–T) for the SLs is also measured as shown in Figure 2f and Figure S4. An identical T_c of ~75 K is obtained for the SLs, where T_c is defined by the zero-crossing temperature of the tangent line (see Figure S4).

Origin of the Interfacial Ferromagnetism in CRO/LNO SLs. The transport measurements above confirm the emergence of the FM phase in the CRO/LNO heterostructure. To reveal the underlying physics of such an interface effect, we studied the valence state and orbital occupation by analyzing the spectra of Ni L-edge, Ru M-edge, and O K-edge, adopting the technique of soft X-ray absorption spectra (XAS) and X-ray linear dichroism (XLD). Since the Ni L_3-edge partially overlaps with the La $M_{4,5}$-edge (see the Supporting Information), we use the Ni L_2-edge to characterize the valence state of Ni. Figure 3a compares the Ni L_2-edge spectrum of the C_n/L_m SL with the reference spectra of the Ni^{3+} ion of LNO bare film and the Ni^{2+} ion of NiO from the literature.[40] Obviously, the shape of the Ni L_2-edge spectrum of the SLs deviates from that of the LNO bare film, exhibiting a low-energy shift and a double-peak structure. A comparison with the reference spectra of Ni^{3+} (a single main peak at 871.6 eV) and Ni^{2+} (double peaks at 870.2 and 871.2 eV) suggests that the Ni ions in the C_n/L_m SL are in a Ni^{3+}/Ni^{2+} mixed valence state. A quantitative analysis of the Ni valence change is given by the relative intensity $I_a/(I_a + I_b)$ of the double peaks a and b as illustrated in Figure 3b (details for the two-peak Gaussian fitting are given in Figure S5b).[41] Obviously, the relative intensity $I_a/(I_a + I_b)$ increases with the increase of n or the decrease of m. It indicates that a thicker CRO sublayer or a thinner LNO sublayer will result in a stronger reduction in Ni valence state.[41] The interfacial charge transfer is also verified by the high-energy shift of the Ru $M_{2,3}$-edges for the C_2/L_2, C_{10}/L_2, and C_{10}/L_6 SLs, compared with that of the CRO bare film (Figure 3c). All of these results indicate that the electrons transfer from Ru ions to Ni ions at the CRO/LNO interface.

Notably, for the SLs with thick CRO or LNO layers, charge transfer may mainly take place in the interface regions, resulting in interfacial phases with distinct properties. A further issue to be addressed is the thickness of each interfacial layer. To determine the range of charge transfer, we further investigated layer-resolved electron energy loss spectra (EELS) around the Ni-L_2 and Ru-L_3 edges. Figure 3d is the enlarged HAADF image of one period of the C_{10}/L_8 SL, where the EELS line profile is conducted in the dashed box along the [001] direction. As shown in Figure 3e, the Ni-L_2 edge exhibits a low-energy shift within two to three Ni–O layers near the interface. Correspondingly, the Ru-L_3 edge in the first one or two Ru–O layers near the interface shifts to high energies (Figure 4f). Thus, the thicknesses of the LNO interfacial layer and CRO-interfacial layer affected by the charge transfer are 2–3 and 1–2 uc, respectively.

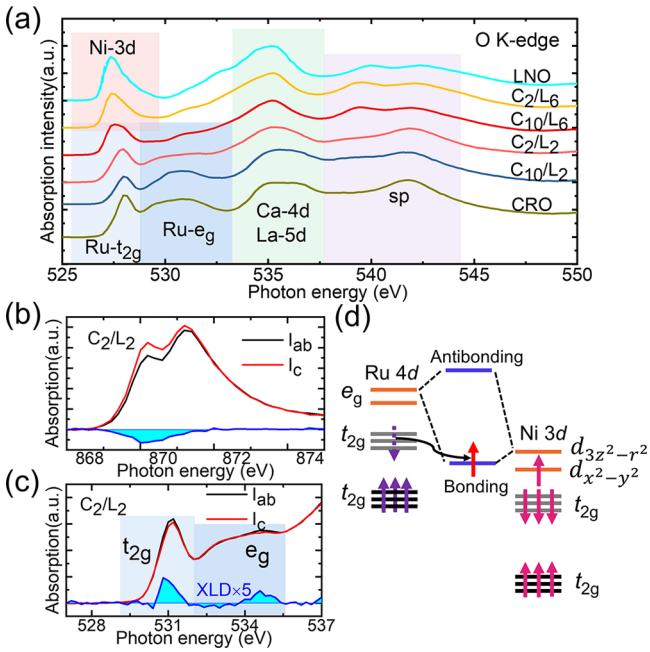

Figure 4. XLD spectra and orbital polarization. (a) Normalized XAS of the O K-edge for the C_n/L_m SLs and reference samples CRO and LNO.[43] Normalized XLD spectra of (b) the Ni L_2-edge and (c) the O K-edge for C_2/L_2 SL, measured with a polarized X-ray beam with different incident angles. The deduced XLD spectra ($I_{ab} - I_c$) are given by the blue line. (d) Schematic of orbital reconstruction and covalent bond at the interface of CRO/LNO.

More features of the SLs are revealed by the XAS spectrum of the O K-edge. Generally, the O K-edge peak stems from the excitation from the O 1s core level to the unoccupied O 2p orbital. The latter is strongly hybridized with the d orbital of transition metal oxides near the Fermi level. In particular, the t_{2g} and e_g metal orbitals have a π-type overlap and a σ-type

https://doi.org/10.1021/acsnano.4c01910
ACS Nano 2024, 18, 9232–9241

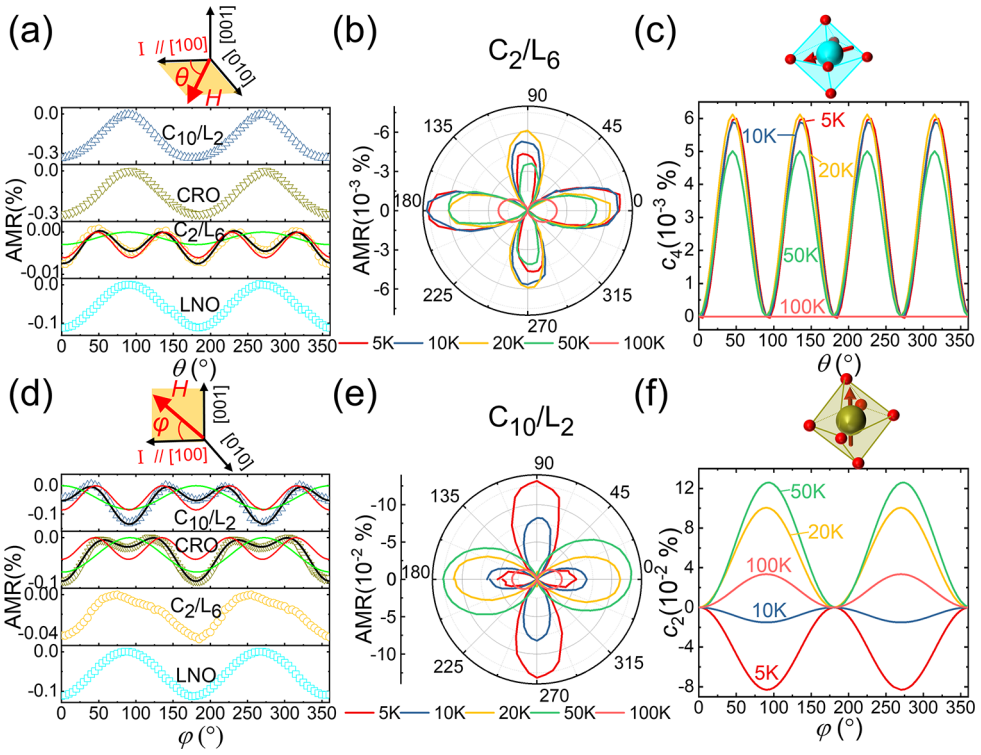

Figure 5. Anisotropic magnetoresistance measurement. (a) AMR measured with a magnetic field of 9 T rotating within the (001) plane at 5 K. The current is always along the [100] direction. θ is the angle between H and the [100] direction. Black solid lines are the results of the curve fitting. Red and green lines are 4-fold and 2-fold components of the AMR, respectively. Top panels show the measurement geometry. (b) Temperature-dependent polar plot of AMR for the C_2/L_6 SL. (c) The extracted 4-fold-symmetry of AMR for the C_2/L_6 SL. The inset is a geometry for the Ni−O octahedron depicting the magnetic easy axis. (d) Angle-dependent AMR measured by a rotating magnetic field (9 T) in the (010) plane at 5 K. φ is the angle between H and the [100] direction. (e) Temperature-dependent polar plot of AMR for the C_{10}/L_2 SL. (f) The extracted 2-fold symmetry of AMR for the C_{10}/L_2 SL. The inset is a geometry for the Ru−O octahedron depicting the magnetic easy axis. For the convenience of comparison, the initial points at θ = 0° or φ = 0° have been aligned for all extracted data.

overlap with the O 2p states, respectively.[42] Thus, the intensity of O K-edge peaks can reflect the number of empty d states. As shown in Figure 4a, there are four resonance peaks around the O K-edge. By comparing the spectra of the SLs with those of the LNO and CRO bare films, we conclude that the peak ranging from 526.9 to 528.7 eV is associated with the Ru t_{2g} orbitals, which partially overlap with the Ni 3d orbitals from 526.3 to 529.9 eV.[43,44] The broad peak ranging from 528.7 to 533.1 eV is related to the Ru e_g orbitals. The peaks ranging from 533.2 to 537.7 eV and from 537.8 to 544.3 eV are derived from the O 2p orbitals mixed with the (La 5d, Ca 4d) and (Ru 5s/5p, Ni 4s/4p) states, respectively. Compared to bare CRO with an empty eg orbital, the reduced intensity of the peak from 528.7 to 533.1 eV for the SLs suggests the partial occupation of the Ru e_g orbitals after the interfacial charge transfer.

According to theoretical calculations, CRO is in close proximity to the PM-FM border of the ruthenate.[26] The positive ordinary Hall coefficient indicates the hole-type charge carriers for the CRO sublayers in the SLs, consistent with previous reports.[45] Thus, the strong Ru to Ni charge transfer increases the hole density in the CRO sublayers. This in turn will enhance the non-spin-polarized density of states ($N(E_F)$) at the Fermi level, resulting in the Stoner criterion $IN(E_F) > 1$ (I is the Stoner parameter) and thus the FM interfacial phase. Furthermore, the charge transfer intermediated by the apical O $2p_z$ orbital forms a Ru−O−Ni covalent bond at the interface, bringing superexchange interactions between the interfacial Ru and Ni ions. Consequently, such interfacial interaction transfers the FM order from the CRO sublayers to the LNO sublayers.

Besides the interfacial FM phases, the formation of the Ru−O−Ni bond also leads to the hybridization of $d_{3z^2-r^2}$ orbitals of Ru and Ni ions, altering the energy band near the Fermi surface. To experimentally check this effect, we performed the XLD studies on the Ni L_2-edge and O K-edge of the C_2/L_2 SL. As illustrated in Figure 4b, the orbital configuration of Ni is probed by the different intensity between I_{ab} (X-ray polarization parallel to in-plane [100]) and I_c (X-ray polarization parallel to out-of-plane [001]). A negative XLD signal ($I_{ab} - I_c$) is observed for the C_2/L_2 SL, indicating the preferred occupation of the $d_{x^2-y^2}$ orbital. The $d_{x^2-y^2}$ orbital polarization is 19%, which is comparable with that of the $LaNiO_3/LaTiO_3$ SL or the $LaNiO_3/DyScO_3$ SL.[40,46] A surprising feature of the XLD spectra on the O K-edge is the presence of e_g polarization of Ru ions in the SL. As shown in Figure 4c, positive XLD peaks are observed in the energy range from 526.9 to 528.7 eV and from 528.7 to 533.1 eV. Since the Ni orbitals are in-plane polarized as already proved, such an out-of-plane polarization should be ascribed to Ru orbitals, i.e., Ru $d_{3z^2-r^2}$ orbitals are preferentially occupied. The hybridization of Ru−O−Ni will form the bonding (lower energy) and antibonding (higher energy) orbitals consisting of $d_{3z^2-r^2}$ orbitals of Ru/Ni ions as shown in Figure 4d. Electrons in the spin-down state of the Ru t_{2g} orbital would transfer to the bonding orbital, resulting in the $d_{3z^2-r^2}$ polarization with the $Ru^{4+\delta}$ valence state. The interfacial

https://doi.org/10.1021/acsnano.4c01910
ACS Nano 2024, 18, 9232−9241

charge transfer also enhances the degeneration of Ru t_{2g} orbitals, as revealed by the XLD peak ranging from 526.9 to 528.7 eV.

Magnetic Anisotropy of CRO/LNO SLs. According to the Bruno model,[47] the spin of the B-site ions of perovskite oxides prefers to align along the direction of orbital momentum. Thus, the different orbital polarization of CRO or LNO sublayers may result in different magnetic anisotropies for the C_n/L_m SL. To get an idea about magnetic anisotropies, we measured the angle-dependent magnetoresistance of the SLs. The anisotropic magnetoresistance is defined by AMR = $\frac{R_\theta - R_{max}}{R_{max}} \times 100\%$, where R_{max} is the maximum resistance and R_θ is the resistance measured with a magnetic field that forms an angle of θ with the current applied along the [100] direction. In Figure 5a, we show the angle-dependent AMR for the C_{10}/L_2 and C_2/L_6 SLs and CRO and LNO bare films, measured at 5 K by a rotating magnetic field (9 T) within the (001) plane. The AMR−θ curves of all SL samples except for C_2/L_6 present 2-fold symmetry with two valleys at θ = 0 and 180°, respectively. The AMR of the C_2/L_6 SL exhibits two oscillations: the first one has the 4-fold-symmetry with four valleys at $\theta = n \times 90°$ (n = 0−3), and the second one has a 2-fold symmetry that is the same as that of other samples. A further feature of the C_2/L_6 SL is revealed by AMR polar plots measured at different temperatures (Figure 5b). The four-petal pattern shrinks with the increase of temperature and turns into a two-petal pattern when $T > T_c$. To get a clear view, we fit the experimental data to the formula of AMR = $c_2 \times \cos(2\theta - \omega_2) + c_4 \times \cos(4\theta - \omega_4)$, where c_2 and c_4 are the amplitudes of 2-fold and 4-fold oscillations, respectively, and ω_2 and ω_4 are the corresponding offset angles. The extracted 4-fold and 2-fold components at varied temperatures are given in Figure 5c and Figure S7. We can see that the 4-fold oscillation shows temperature dependence very similar to that of the $\sigma_{xy}^{AHE}-T$ curve in Figure 2f: its amplitude first keeps constant in the temperature range of 5−20 K and then begins to drop at 50 K and finally disappears above 100 K. It strongly suggests that the 4-fold AMR stems from the magnetic contributions, i.e. the magnetic easy axis of the C_2/L_6 SL lies along the in-plane [100] or [010] directions, where the AMR valleys appear due to the minimal spin-flip scattering when spins are fully aligned along the applied field. This is reasonable since the AMR of the C_2/L_6 SL is determined by the dominant LNO sublayers, which exhibit a preferred occupation of the $d_{x^2-y^2}$ orbital, as mentioned above.

For the C_{10}/L_2 SL with dominant CRO sublayers, the AMR with H rotating in the (001)-plane only demonstrates the normal 2-fold oscillation that is usually ascribed to normal AMR or Lorentz scattering. However, it becomes different when H rotates in the (010) plane. As shown in Figure 5d, the AMR−φ curve of the C_{10}/L_2 SL consists of two oscillations with the 4-fold symmetry and 2-fold symmetry, respectively.

Here the 4-fold oscillation is unlikely to be contributed by magnetic anisotropy since it is also observed in the CRO bare film. This is similar to previous work on a CRO film, where the 4-fold crystal symmetry of CRO is believed to the origin of 4-fold AMR oscillation.[48,49] The interesting thing is, as shown in Figure 5e,f, the 2-fold oscillation of the C_{10}/L_2 SL shows two valleys at φ = 90 and 270° at 5 K and turns to two peaks at the same position when temperature exceeds 20 K. Such an inversion indicates that the 2-fold AMR term is determined by the competition of two origins: one comes from the nonmagnetic contributions with the maximum resistance at φ = 90 and 270° the same as for the CRO and LNO bare films, and another comes from the magnetic contribution with the minimal resistance at φ = 90 and 270° that dramatically decreases with the increase of temperature. In other words, the C_{10}/L_2 SL has perpendicular magnetic anisotropy at low temperatures, consistent with the preferred $d_{3z^2-r^2}$ orbital occupation of CRO sublayers. The above results reveal the out-of-plane magnetic anisotropy for the CRO-dominant SL and the in-plane magnetic anisotropy for the LNO-dominant SL. As a supplement, in Figure S4, we give the $M-H$ curves measured in different directions for the C_{10}/L_2 and C_2/L_6 SLs, well supporting the AMR results. Naturally, the different magnetic anisotropies of CRO and LNO sublayers will result in competition, allowing us to align the spins of Ru/Ni ions in the C_n/L_m SL by adopting appropriate n/m combinations. This has potential applications in low-power consumption or exchange spring devices.[50−52]

CONCLUSION

In summary, we fabricated a series of high-quality CRO/LNO SLs with different thickness combinations. The Hall and MR measurements indicate the emergence of a ferromagnetic phase in either CRO or LNO sublayers. XAS suggests a notable charge transfer from Ru to Ni at the interface, leading to the strong exchange interaction between the Ru/Ni ions and thus the ferromagnetic order. Moreover, the CRO-dominant or LNO-dominant SLs demonstrate distinct magnetic anisotropy, which is related to the different orbital polarization of CRO or LNO sublayers, as revealed by the XLD spectra. Our work provides a feasible way to induce and tune ferromagnetic orders in the oxide heterostructures composed of PM/PM materials, implying potential applications in spintronics and magnetoelectronics.

METHODS

Sample Synthesis. High-quality C_n/L_m SLs were epitaxially grown on single-crystalline (001)-oriented LSAT substrates by pulsed laser deposition (KrF, λ = 248 nm) with 10 repetitions, where n = 2, 10 and m = 2, 4, 6, 8 represent the numbers of unit cells for the CRO and LNO sublayers, respectively. CRO and LNO bare films were also prepared for comparison. In the growth process, the substrate was kept at 680 °C and the oxygen pressure was set to 40 Pa. The fluence of the laser pulse was 1.2 J/cm^2, and the repetition rate was 2 Hz. After deposition, the sample was cooled to room temperature with an oxygen pressure of 100 Pa. The deposition rate of each film was carefully calibrated by the technique of small-angle X-ray reflectivity (XRR), and the thickness of sublayers was precisely controlled by counting the pulse number.

Sample Characterization. The surface morphology was measured with an atomic force microscope (AFM) (SPI 3800N, Seiko). The crystal structure was determined with a high-resolution X-ray diffractometer (D8 Discover, Bruker) with Cu Kα radiation. Atomic-scale lattice images were recorded by high-resolution scanning transmission electron microscopy (STEM) with double CS correctors (Thermo Fisher Spectra 300). Cross-sectional thin samples for STEM analysis were prepared by using a dual-beam focused ion beam system along the [100] direction. The magnetic properties were measured by a Quantum Design vibrating sample magnetometer (VSM-SQUID) in the temperature range 5−200 K, with a magnetic field of 0.2 T in field-cooling mode. The magnetic field was applied along the out-of-plane direction of the (001) films. The transport measurements were performed in a Quantum Design physical property measurement system (PPMS) with standard Hall bar geometry. The Hall bar devices have a width of 200 μm and a length of 1200 μm, fabricated

https://doi.org/10.1021/acsnano.4c01910
ACS Nano 2024, 18, 9232−9241

by conventional lithography and Ar-ion etching techniques. Aluminum wires, 20 μm in diameter, were employed to establish the connections between the sample and the electrodes, via ultrasound-assisted wire bonding. The schematic view of the experimental setup for Hall measurements is shown in the inset of Figure 2b. A DC current of 100 μA was applied along the in-plane [100] direction, and the magnetic field was applied along the out-of-plane [001] direction.

XAS Measurement. The XAS measurements were performed at the BL08U1A beamline at the Shanghai Synchrotron Radiation Facility. The measurements took place at room temperature and employed a total-electron-yield mode. The XLD spectra were obtained by two polarization directions of linearly polarized X-rays, which were achieved by rotating the X-ray incidence angle, with values of 90 and 30° corresponding to the IP direction ($E\|a$ or b, I_{ab}) and the OP direction ($E\|c$, I_c), respectively, where E is the electric field of the X-rays, a, b, and c are the axes of the sample, and I_{ab} and I_c are the absorption intensities along the corresponding directions. The XLD value was calculated as the difference between the two measurements, namely, $I_{ab} - I_c$.

ASSOCIATED CONTENT

Supporting Information

The Supporting Information is available free of charge at https://pubs.acs.org/doi/10.1021/acsnano.4c01910.

Magnetic and transport characterization of LNO (10 nm in thickness) and CRO (8 nm in thickness) bare films, MR curves of C_{10}/L_2 and C_2/L_6 SLs, $\Delta\rho_{xy}^{AHE}(T)-\rho_{xx}^2(T)$ curves, $M-T$ and $M-H$ curves of C_n/L_m SLs, normalized XAS spectra of the Ni $L_{2,3}$-edge and the Ru $M_{2,3}$-edge, normalized XLD spectra of the O K-edge for a CRO bare film, and angle-dependent AMR of C_{10}/L_2 and C_2/L_6 SLs (PDF)

AUTHOR INFORMATION

Corresponding Authors

Jing Zhang − *Songshan Lake Materials Laboratory, Dongguan, Guangdong 523808, People's Republic of China*; Email: zhangjing@sslab.org.cn

Yuansha Chen − *Beijing National Laboratory for Condensed Matter Physics and Institute of Physics, Chinese Academy of Sciences, Beijing 100190, People's Republic of China; School of Physical Sciences, University of Chinese Academy of Sciences, Beijing 100049, People's Republic of China*; Email: yschen@iphy.ac.cn

Jirong Sun − *Beijing National Laboratory for Condensed Matter Physics and Institute of Physics, Chinese Academy of Sciences, Beijing 100190, People's Republic of China; School of Physical Sciences, University of Chinese Academy of Sciences, Beijing 100049, People's Republic of China; Spintronics Institute, School of Physics and Technology, University of Jinan, Jinan 250022, China*; orcid.org/0000-0003-4531-4794; Email: jrsun@iphy.ac.cn

Authors

Jie Zheng − *Beijing National Laboratory for Condensed Matter Physics and Institute of Physics, Chinese Academy of Sciences, Beijing 100190, People's Republic of China; School of Physical Sciences, University of Chinese Academy of Sciences, Beijing 100049, People's Republic of China*

Wenxiao Shi − *Beijing National Laboratory for Condensed Matter Physics and Institute of Physics, Chinese Academy of Sciences, Beijing 100190, People's Republic of China; School of Physical Sciences, University of Chinese Academy of Sciences, Beijing 100049, People's Republic of China*

Zhe Li − *Beijing National Laboratory for Condensed Matter Physics and Institute of Physics, Chinese Academy of Sciences, Beijing 100190, People's Republic of China; School of Physical Sciences, University of Chinese Academy of Sciences, Beijing 100049, People's Republic of China*

Chao-Yao Yang − *Department of Materials Science and Engineering, National Yang Ming Chiao Tung University, Hsinchu 300, Taiwan*

Zhaozhao Zhu − *Beijing National Laboratory for Condensed Matter Physics and Institute of Physics, Chinese Academy of Sciences, Beijing 100190, People's Republic of China; School of Physical Sciences, University of Chinese Academy of Sciences, Beijing 100049, People's Republic of China*; orcid.org/0000-0002-6500-0242

Mengqin Wang − *Beijing National Laboratory for Condensed Matter Physics and Institute of Physics, Chinese Academy of Sciences, Beijing 100190, People's Republic of China; School of Physical Sciences, University of Chinese Academy of Sciences, Beijing 100049, People's Republic of China*

Jine Zhang − *School of Integrated Circuit Science and Engineering, Beihang University, Beijing 100191, People's Republic of China*

Furong Han − *School of Integrated Circuit Science and Engineering, Beihang University, Beijing 100191, People's Republic of China*

Hui Zhang − *School of Integrated Circuit Science and Engineering, Beihang University, Beijing 100191, People's Republic of China*

Yunzhong Chen − *Beijing National Laboratory for Condensed Matter Physics and Institute of Physics, Chinese Academy of Sciences, Beijing 100190, People's Republic of China; School of Physical Sciences, University of Chinese Academy of Sciences, Beijing 100049, People's Republic of China*; orcid.org/0000-0001-8368-5823

Fengxia Hu − *Beijing National Laboratory for Condensed Matter Physics and Institute of Physics, Chinese Academy of Sciences, Beijing 100190, People's Republic of China; School of Physical Sciences, University of Chinese Academy of Sciences, Beijing 100049, People's Republic of China*; orcid.org/0000-0003-0383-0213

Baogen Shen − *Beijing National Laboratory for Condensed Matter Physics and Institute of Physics, Chinese Academy of Sciences, Beijing 100190, People's Republic of China; School of Physical Sciences, University of Chinese Academy of Sciences, Beijing 100049, People's Republic of China; Ningbo Institute of Materials Technology & Engineering, Chinese Academy of Sciences, Ningbo, Zhejiang 315201, People's Republic of China*; orcid.org/0000-0003-4819-1806

Complete contact information is available at: https://pubs.acs.org/10.1021/acsnano.4c01910

Notes

The authors declare no competing financial interest.

ACKNOWLEDGMENTS

This work has been supported by the National Key R&D Program of China (2023YFA1607400, 2022YFA1403302, and 2019YFA0704904), the Science Center of the National Science Foundation of China (52088101), the National Natural Science Foundation of China (11934016, 12274443,

T2394472, and 12304149) and the Key Program of the Chinese Academy of Sciences (XDB33030200). Jirong Sun acknowledges the support of the Project for Innovative Research Team of National Natural Science Foundation of China (11921004). Jing Zhang acknowledges the support of the Guangdong Basic and Applied Basic Research Foundation (2022A1515110648 and 2023A1515010953). We acknowledge Beamline BL08U1A and BL02U2 at the Shanghai Synchrotron Radiation Facility (SSRF) for the XAS characterizations and the Synergetic Extreme Condition User Facility (SECUF) for the Hall effect characterizations.

REFERENCES

(1) Takagi, H.; Hwang, H. Y. An Emergent Change of Phase for Electronics. *Science* **2010**, *327*, 1601−1602.
(2) Dagotto, E. Complexity in Strongly Correlated Electronic Systems. *Science* **2005**, *309*, 257−262.
(3) Uehara, M.; Mori, S.; Chen, C. H.; Cheong, S.-W. Percolative Phase Separation Underlies Colossal Magnetoresistance in Mixed-Valent Manganites. *Nature* **1999**, *399*, 560−563.
(4) Wang, J.; Neaton, J. B.; Zheng, H.; Nagarajan, V.; Ogale, S. B.; Liu, B.; Viehland, D.; Vaithyanathan, V.; Schlom, D. G.; Waghmare, U. V.; Spaldin, N. A.; Rabe, K. M.; Wuttig, M.; Ramesh, R. Epitaxial $BiFeO_3$ Multiferroic Thin Film Heterostructures. *Science* **2003**, *299*, 1719−1722.
(5) Brahlek, M.; Gupta, A. S.; Lapano, J.; Roth, J.; Zhang, H.; Zhang, L.; Haislmaier, R.; Engel-Herbert, R. Frontiers in the Growth of Complex Oxide Thin Films: Past, Present, and Future of Hybrid MBE. *Adv. Funct. Mater.* **2018**, *28*, No. 1702772.
(6) Hwang, H. Y.; Iwasa, Y.; Kawasaki, M.; Keimer, B.; Nagaosa, N.; Tokura, Y. Emergent Phenomena at Oxide Interfaces. *Nat. Mater.* **2012**, *11*, 103−113.
(7) He, C.; Grutter, A. J.; Gu, M.; Browning, N. D.; Takamura, Y.; Kirby, B. J.; Borchers, J. A.; Kim, J. W.; Fitzsimmons, M. R.; Zhai, X.; Mehta, V. V.; Wong, F. J.; Suzuki, Y. Interfacial Ferromagnetism and Exchange Bias in $CaRuO_3/CaMnO_3$ Superlattices. *Phys. Rev. Lett.* **2012**, *109*, No. 197202.
(8) Chen, Z.; Liu, Y.; Zhang, H.; Liu, Z.; Tian, H.; Sun, Y.; Zhang, M.; Zhou, Y.; Sun, J.; Xie, Y. Electric Field Control of Superconductivity at the $LaAlO_3/KTaO_3$ (111). *Interface. Science* **2021**, *372*, 721−724.
(9) Liu, X.; Kotiuga, M.; Kim, H.-S.; N'Diaye, A. T.; Choi, Y.; Zhang, Q.; Cao, Y.; Kareev, M.; Wen, F.; Pal, B.; Freeland, J. W.; Gu, L.; Haskel, D.; Shafer, P.; Arenholz, E.; Haule, K.; Vanderbilt, D.; Rabe, K. M.; Chakhalian, J. Interfacial Charge-Transfer Mott State in Iridate−Nickelate Superlattices. *Proc. Natl. Acad. Sci. U.S.A.* **2019**, *116*, 19863−19868.
(10) Song, J.; Chen, Y.; Chen, X.; Khan, T.; Han, F.; Zhang, J.; Huang, H.; Zhang, H.; Shi, W.; Qi, S.; Hu, F.; Shen, B.; Sun, J. Electric Tuning of Magnetic Anisotropy and Exchange Bias of $La_{0.8}Sr_{0.2}CoO_3/La_{0.67}Sr_{0.33}MnO_3$ Bilayer Films. *Phys. Rev. Appl.* **2020**, *14*, No. 024062.
(11) Ohtomo, A.; Hwang, H. Y. A High-Mobility Electron Gas at the $LaAlO_3/SrTiO_3$ Heterointerface. *Nature* **2004**, *427*, 423−426.
(12) Anderson, P. W. Antiferromagnetism. Theory of Superexchange Interaction. *Phys. Rev.* **1950**, *79*, 350−356.
(13) Goodenough, J. B. Theory of the Role of Covalence in the Perovskite-Type Manganites [La,M(II)]MnO_3. *Phys. Rev.* **1955**, *100*, 564−573.
(14) Kanamori, J. Superexchange Interaction and Symmetry Properties of Electron Orbitals. *J. Phys. Chem. Solids* **1959**, *10*, 87−98.
(15) Yoo, M.-W.; Tornos, J.; Sander, A.; Lin, L.-F.; Mohanta, N.; Peralta, A.; Sanchez-Manzano, D.; Gallego, F.; Haskel, D.; Freeland, J. W.; Keavney, D. J.; Choi, Y.; Strempfer, J.; Wang, X.; Cabero, M.; Vasili, H. B.; Valvidares, M.; Sanchez-Santolino, G.; Gonzalez-Calbet, J. M.; Rivera, A.; et al. Large Intrinsic Anomalous Hall Effect in $SrIrO_3$ Induced by Magnetic Proximity Effect. *Nat. Commun.* **2021**, *12*, 3283.
(16) Jaiswal, A. K.; Wang, D.; Wollersen, V.; Schneider, R.; Tacon, M. L.; Fuchs, D. Direct Observation of Strong Anomalous Hall Effect and Proximity-Induced Ferromagnetic State in $SrIrO_3$. *Adv. Mater.* **2022**, *34*, No. 2109163.
(17) Gibert, M.; Zubko, P.; Scherwitzl, R.; Íñiguez, J.; Triscone, J.-M. Exchange Bias in $LaNiO_3$-$LaMnO_3$ Superlattices. *Nat. Mater.* **2012**, *11*, 195−198.
(18) Nichols, J.; Gao, X.; Lee, S.; Meyer, T. L.; Freeland, J. W.; Lauter, V.; Yi, D.; Liu, J.; Haskel, D.; Petrie, J. R.; Guo, E.-J.; Herklotz, A.; Lee, D.; Ward, T. Z.; Eres, G.; Fitzsimmons, M. R.; Lee, H. N. Emerging Magnetism and Anomalous Hall Effect in Iridate−Manganite Heterostructures. *Nat. Commun.* **2016**, *7*, 12721.
(19) Grutter, A. J.; Vailionis, A.; Borchers, J. A.; Kirby, B. J.; Flint, C. L.; He, C.; Arenholz, E.; Suzuki, Y. Interfacial Symmetry Control of Emergent Ferromagnetism at the Nanoscale. *Nano Lett.* **2016**, *16*, 5647−5651.
(20) Grutter, A. J.; Yang, H.; Kirby, B. J.; Fitzsimmons, M. R.; Aguiar, J. A.; Browning, N. D.; Jenkins, C. A.; Arenholz, E.; Mehta, V. V.; Alaan, U. S.; Suzuki, Y. Interfacial Ferromagnetism in $LaNiO_3/CaMnO_3$ Superlattices. *Phys. Rev. Lett.* **2013**, *111*, No. 087202.
(21) Shi, W.; Zheng, J.; Li, Z.; Wang, M.; Zhu, Z.; Zhang, J.; Zhang, H.; Chen, Y.; Hu, F.; Shen, B.; Chen, Y.; Sun, J. Enhancing Interfacial Ferromagnetism and Magnetic Anisotropy of $CaRuO_3/SrTiO_3$ Superlattices *via* Substrate Orientation. *Small* **2023**, *19*, No. 2308172.
(22) Shi, W.; Zhang, J.; Chen, X.; Zhang, Q.; Zhan, X.; Li, Z.; Zheng, J.; Wang, M.; Han, F.; Zhang, H.; Gu, L.; Zhu, T.; Liu, B.; Chen, Y.; Hu, F.; Shen, B.; Chen, Y.; Sun, J. Symmetry-Mismatch-Induced Ferromagnetism in the Interfacial Layers of $CaRuO_3/SrTiO_3$ Superlattices. *Adv. Funct. Mater.* **2023**, *33*, No. 2300338.
(23) Mazin, I. I.; Singh, D. J. Electronic Structure and Magnetism in Ru-Based Perovskites. *Phys. Rev. B* **1997**, *56*, 2556−2571.
(24) Maiti, K. Role of Covalency in the Ground-State Properties of Perovskite Ruthenates: A First-Principles Study Using Local Spin Density Approximations. *Phys. Rev. B* **2006**, *73*, No. 235110.
(25) Shepard, M.; McCall, S.; Cao, G.; Crow, J. E. Thermodynamic Properties of Perovskite $ARuO_3$ (A = Ca, Sr, and Ba) Single. *Crystals. J. Appl. Phys.* **1997**, *81*, 4978−4980.
(26) Cao, G.; McCall, S.; Shepard, M.; Crow, J. E.; Guertin, R. P. Thermal, Magnetic, and Transport Properties of Single-Crystal $Sr_{1-x}Ca_xRuO_3$ ($0 \leq x \leq 1.0$). *Phys. Rev. B* **1997**, *56*, 321.
(27) Rajeev, K. P.; Shivashankar, G. V.; Raychaudhuri, A. K. Low-Temperature Electronic Properties of a Normal Conducting Perovskite Oxide ($LaNiO_3$). *Solid State Commun.* **1991**, *79*, 591−595.
(28) Catalano, S.; Gibert, M.; Fowlie, J.; Íñiguez, J.; Triscone, J.-M.; Kreisel, J. Rare-Earth Nickelates $RNiO_3$: Thin Films and Heterostructures. *Rep. Prog. Phys.* **2018**, *81*, No. 046501.
(29) Torrance, J.; Lacorre, P.; Nazzal, A.; Ansaldo, E.; Niedermayer, Ch. Systematic Study of Insulator-Metal Transitions in Perovskites $RNiO_3$ (R = Pr,Nd,Sm,Eu) Due to Closing of Charge-Transfer Gap. *Phys. Rev. B* **1992**, *45*, 8209−8212.
(30) Gibert, M.; Viret, M.; Zubko, P.; Jaouen, N.; Tonnerre, J.-M.; Torres-Pardo, A.; Catalano, S.; Gloter, A.; Stéphan, O.; Triscone, J.-M. Interlayer Coupling through a Dimensionality-Induced Magnetic State. *Nat. Commun.* **2016**, *7*, 11227.
(31) Lee, A. T.; Han, M. J. Charge Transfer, Confinement, and Ferromagnetism in $LaMnO_3/LaNiO_3$ (001) Superlattices. *Phys. Rev. B* **2013**, *88*, No. 035126.
(32) Hyun, S.; Cho, J. H.; Kim, A.; Kim, J.; Kim, T.; Char, K. Coexistence of Metallic and Insulating Phases in Epitaxial $CaRuO_3$ Thin Films Observed by Scanning Microwave Microscopy. *Appl. Phys. Lett.* **2002**, *80*, 1574−1576.
(33) Ali, Z.; Saghayezhian, M.; Wang, Z.; O'Hara, A.; Shin, D.; Ge, W.; Chan, Y. T.; Zhu, Y.; Wu, W.; Pantelides, S. T.; Zhang, J. Emergent Ferromagnetism and Insulator-Metal Transition in δ-Doped Ultrathin Ruthenates. *npj Quantum Mater.* **2022**, *7*, 108.
(34) Scherwitzl, R.; Zubko, P.; Lichtensteiger, C.; Triscone, J.-M. Electric-Field Tuning of the Metal-Insulator Transition in Ultrathin Films of $LaNiO_3$. *Appl. Phys. Lett.* **2009**, *95*, No. 222114.

https://doi.org/10.1021/acsnano.4c01910
ACS Nano 2024, 18, 9232−9241

(35) Scherwitzl, R.; Gariglio, S.; Gabay, M.; Zubko, P.; Gibert, M.; Triscone, J.-M. Metal-Insulator Transition in Ultrathin $LaNiO_3$ Films. *Phys. Rev. Lett.* **2011**, *106*, No. 246403.
(36) Wei, H.; Jenderka, M.; Bonholzer, M.; Grundmann, M.; Lorenz, M. Modeling the Conductivity around the Dimensionality-Controlled Metal-Insulator Transition in $LaNiO_3/LaAlO_3$ (100) Superlattices. *Appl. Phys. Lett.* **2015**, *106*, No. 042103.
(37) May, S. J.; Santos, T. S.; Bhattacharya, A. Onset of Metallic Behavior in Strained $(LaNiO_3)_n/(SrMnO_3)_2$ Superlattices. *Phys. Rev. B* **2009**, *79*, No. 115127.
(38) Nagaosa, N.; Sinova, J.; Onoda, S.; MacDonald, A. H.; Ong, N. P. Anomalous Hall Effect. *Rev. Mod. Phys.* **2010**, *82*, 1539−1592.
(39) Onoda, S.; Sugimoto, N.; Nagaosa, N. Intrinsic Versus Extrinsic Anomalous Hall Effect in Ferromagnets. *Phys. Rev. Lett.* **2006**, *97*, No. 126602.
(40) Cao, Y.; Liu, X.; Kareev, M.; Choudhury, D.; Middey, S.; Meyers, D.; Kim, J.-W.; Ryan, P. J.; Freeland, J. W.; Chakhalian, J. Engineered Mott Ground State in a $LaTiO_{3+\delta}/LaNiO_3$ Heterostructure. *Nat. Commun.* **2016**, *7*, 10418.
(41) Grisolia, M. N.; Varignon, J.; Sanchez-Santolino, G.; Arora, A.; Valencia, S.; Varela, M.; Abrudan, R.; Weschke, E.; Schierle, E.; Rault, J. E.; Rueff, J.-P.; Barthélémy, A.; Santamaria, J.; Bibes, M. Hybridization-Controlled Charge Transfer and Induced Magnetism at Correlated Oxide Interfaces. *Nat. Phys.* **2016**, *12*, 484−492.
(42) Frati, F.; Hunault, M. O. J. Y.; De Groot, F. M. F. Oxygen K-Edge X-Ray Absorption Spectra. *Chem. Rev.* **2020**, *120*, 4056−4110.
(43) Abbate, M.; Zampieri, G.; Prado, F.; Caneiro, A.; Gonzalez-Calbet, J. M.; Vallet-Regi, M. Electronic Structure and Metal-Insulator Transition in $LaNiO_{3-\delta}$. *Phys. Rev. B* **2002**, *65*, No. 155101.
(44) Manica, J.; Abbate, M.; Gayone, J. E.; Guevara, J. A.; Cuffini, S. L. O 1s X-Ray Absorption Spectra and Band Structure Calculations of $Ca_{1-x}Sr_xRuO_3$. *J. Alloys Compd.* **2004**, *377*, 25−28.
(45) Shen, S.; Li, Z.; Tian, Z.; Luo, W.; Okamoto, S.; Yu, P. Emergent Ferromagnetism with Fermi-Liquid Behavior in Proton Intercalated $CaRuO_3$. *Phys. Rev. X* **2021**, *11*, No. 021018.
(46) Wu, M.; Benckiser, E.; Haverkort, M. W.; Frano, A.; Lu, Y.; Nwankwo, U.; Brück, S.; Audehm, P.; Goering, E.; Macke, S.; Hinkov, V.; Wochner, P.; Christiani, G.; Heinze, S.; Logvenov, G.; Habermeier, H.-U.; Keimer, B. Strain and Composition Dependence of Orbital Polarization in Nickel Oxide Superlattices. *Phys. Rev. B* **2013**, *88*, No. 125124.
(47) Bruno, P. Tight-Binding Approach to the Orbital Magnetic Moment and Magnetocrystalline Anisotropy of Transition-Metal Monolayers. *Phys. Rev. B* **1989**, *39*, 865−868.
(48) Schultz, M.; Klein, L.; Reiner, J. W.; Beasley, M. R. Uniaxial Magnetocrystalline Anisotropy in $CaRuO_3$. *Phys. Rev. B* **2006**, *73*, No. 085109.
(49) Proffit, D. L.; Jang, H. W.; Lee, S.; Nelson, C. T.; Pan, X. Q.; Rzchowski, M. S.; Eom, C. B. Influence of Symmetry Mismatch on Heteroepitaxial Growth of Perovskite Thin Films. *Appl. Phys. Lett.* **2008**, *93*, No. 111912.
(50) Huang, Y.; Yang, C.; Cheng, C.; Lee, A.; Tseng, C.; Wu, H.; Pan, Q.; Che, X.; Lai, C.; Wang, K.; Lin, H.; Tseng, Y. A Spin-Orbit Torque Ratchet at Ferromagnet/Antiferromagnet Interface *via* Exchange Spring. *Adv. Funct. Mater.* **2022**, *32*, No. 2111653.
(51) Koch, M. M.; Bergmann, L.; Agrestini, S.; Maznichenko, I.; Mertig, I.; Herklotz, A.; Das, S.; Rata, D. A.; Dörr, K. Thickness-Dependent Ru Exchange Spring at $La_{0.7}Sr_{0.3}MnO_3$−$SrRuO_3$ Interface. *Phys. Status Solidi B* **2020**, *257*, No. 1900616.
(52) Wang, Y.; Zhou, X.; Song, C.; Yan, Y.; Zhou, S.; Wang, G.; Chen, C.; Zeng, F.; Pan, F. Electrical Control of the Exchange Spring in Antiferromagnetic Metals. *Adv. Mater.* **2015**, *27*, 3196−3201.

https://doi.org/10.1021/acsnano.4c01910
ACS Nano 2024, 18, 9232−9241